Square-Root Higher-Order Topology in Rectangular-Lattice Acoustic Metamaterials

Shi-Qiao Wu,[1,*] Zhi-Kang Lin,[1] Zhan Xiong,[2] Bin Jiang,[1] and Jian-Hua Jiang[1,†]

[1]*Institute of Theoretical and Applied Physics, School of Physical Science and Technology & Collaborative Innovation Center of Suzhou Nano Science and Technology, Soochow University, 1 Shizi Street, Suzhou, 215006, China*

[2]*College of Physics and Electronic Information Engineering, Zhejiang Normal University, Jinhua, Zhejiang 321004, China*

Square-root topology offers a distinctive scheme towards topological phases with unconventional spectral properties. In many cases, the formation of square-root topology is governed by the inherent lattice symmetry, with honeycomb lattices being prominent examples. Here, we report on the experimental discovery of square-root higher-order topological insulator phases in an acoustic metamaterial with decorated rectangular lattice. Through acoustic pump-probe techniques, we explore the boundary-dependent topological edge and corner states in both the parent and square-root acoustic metamaterials. We further validate their higher-order topologies as well as their spectral connections via various simulations. Our work not only substantiates the square-root higher-order topology in rectangular-lattice systems from the experimental aspect, but also serves as a step towards versatile higher-order topological phenomena in photonic, acoustic, and mechanical metamaterials.

I. INTRODUCTION

Since the discovery of the quantum Hall effect [1], the study of topological states of matter has greatly expanded the scope of phases of matter and their phase transitions [2,3]. The recently discovered higher-order topological phases further enrich the physics of topological materials, extending the celebrated bulk-edge correspondence to the multidimensional bulk-edge-corner, bulk-surface-hinge, and bulk-surface-hinge-corner correspondences [4–30]. Since their naissance, higher-order topological insulators have not only been studied extensively in solid-state systems [13–16], but also been explored in metamaterials for photonic [19,25,29], acoustic [18,20,22], mechanical [17], and other classical waves. The macroscopic nature of these metamaterials enables feasible control and extraordinary abilities to detect the spectral and eigenstates' properties with excellent frequency and spatial resolutions. Furthermore, the study of topological phenomena in metamaterials could enable or improve cutting-edge applications and technologies.

Recently, an unusual approach, termed the square-root topology, was developed as another route toward unconventional topological states of matter [31–45]. In square-root topological insulators (SRTIs) and semimetals, the square-root lattices are often generated by inserting additional sites into their parent lattices. Through a geometrical relation between the parent lattice and the SRTI, their spectra are also intimately connected: the spectrum of the SRTI is the doubled form of the spectrum of the parent lattice. As a consequence, the topological edge and corner states around zero energy are doubly copied and transferred to the bulk band gaps above and below zero energy.

The intriguing spectral connection between the SRTI and the parent lattice has stimulated experimental research on SRTIs based on honeycomb-lattice systems [33,34,39,41]. However, to date, SRTIs based on rectangular lattices have not yet been explored in experiments. A recent theoretical study unveiled the interesting properties of SRTIs in rectangular-lattice systems with further generalization even to quarter-root topological phases [38], indicating that SRTIs in rectangular lattices hold promise for rich topological phases and phenomena.

Here, we report on the experimental observation of SRTIs in two-dimensional (2D) rectangular-lattice acoustic metamaterials. We achieve the experimental realization of the parent and descendant models of the SRTIs using designer acoustic metamaterials [46–49] based on coupled acoustic cavities. In our scheme, a complete acoustic band gap with a band-gap-to-mid-gap ratio of approximately 10% in the parent acoustic metamaterial, and two complete acoustic band gaps with band-gap-to-mid-gap ratio of around 8% in the square-root acoustic metamaterial are

———————
*wushiqiao4570@gmail.com
†jianhuajiang@suda.edu.cn

realized. These large complete acoustic band gaps give access to the observation of the square-root topological phenomena in our systems. Furthermore, the square-root topological states in rectangular lattices give rise to rich topological edge and corner states. For the systems studied here, the edge states emerging in different band gaps are localized at different edge boundaries, either the horizontal or the vertical edge boundaries. As a consequence, the doubling of the spectrum of the parent model in the square-root topological system is even richer. These phenomena were not observed in the square-root topological systems investigated in previous experimental works [32,33]. Here, we demonstrate in both experiments and simulations that higher-order topological features, such as the topological edge and corner states, emerge in both the SRTI and the parent lattice. In fact, the spectral features in the SRTI and its parent lattice are connected via the square-root construction. Such a connection is verified via the spectral and wave-function properties of the topological edge and corner states in the SRTI and its parent lattice. Furthermore, the robustness of the topological boundary states is confirmed by examining the effect of defects in various configurations. Here, the observed connection between the SRTI and its parent lattice, together with the emergent topological edge and corner states in these systems, as well as their acoustic realizations, unveil the intriguing interplay between the higher-order band topology and the square-root construction.

II. SQUARE-ROOT MODEL

Here, we use the tight-binding models of the SRTI and its parent lattice to illustrate the square-root topological principle. We first introduce the parent lattice, a generalized 2D rectangular-lattice Su-Schrieffer-Heeger (SSH) model with anisotropic nearest-neighbor couplings illustrated in Fig. 1(a). This model is described by the following Bloch Hamiltonian after Fourier transformation,

$$H_{\text{original}} = \begin{bmatrix} 0 & h_{\text{original}}^{\dagger} \\ h_{\text{original}} & 0 \end{bmatrix}, \quad (1)$$

where

$$h_{\text{original}} = \begin{bmatrix} t_{1x} + t_{2x}e^{ik_x} & t_{1y} + t_{2y}e^{ik_y} \\ t_{1y} + t_{2y}e^{-ik_y} & t_{1x} + t_{2x}e^{-ik_x} \end{bmatrix}. \quad (2)$$

k_x and k_y are the Bloch wave vectors along x and y directions, respectively. Without loss of generality, the lattice constant is set as unity. $t_{i\mu}$ ($i = 1, 2$) denotes the intracell and intercell couplings between the nearest-neighboring sites, respectively, where $\mu = x, y$ represents the hopping along the x and y directions, respectively. The pale yellow squares in Fig. 1(a) indicate the primitive unit cell. Each unit cell has four sites. The green (pink) lines indicate

the horizontal (vertical) hopping along the x (y) direction, and the single (double) lines depict the weak (strong) couplings.

For concreteness, in the tight-binding model, two hopping parameters are chosen as $t_{2x} = 1$ and $t_{2y} = 0.2$. The energy spectra of a system with 4×4 unit cells are plotted as a function of the intracell hopping t_{1x} in Fig. 1(b) at the condition with $t_{1y} = t_{1x}$. According to Ref. [38], when $t_{1x} = t_{1y} < 0.34$, the system is in the topological phase and various topological boundary states emerge. For instance, when $t_{1x} = t_{1y} = 0.1$, there are topological corner states at zero energy (red curves) as well as horizontal (blue curves) and vertical edge states (green curves) at finite energies. Interestingly, here, the vertical edge states are located in the central bulk band gap, whereas the horizontal edge states emerge in the two smaller bulk band gaps above and below, due to the different hoppings along the x and y directions in this model. These features are quite different from the topological phenomena in existing higher-order topological insulators.

The tight-binding model of the descendant SRTI, illustrated in Fig. 1(c), is created by adding a site at the middle of each pair of nearest-neighboring sites in the parent model and transforming the nearest-neighbor couplings from $t_{i\mu}$ to $\sqrt{t_{i\mu}}$. The resultant descendant model is described by the following Hamiltonian:

$$H_{\text{root}} = \begin{bmatrix} 0 & h_{\text{root}}^{\dagger} \\ h_{\text{root}} & 0 \end{bmatrix}, \quad (3)$$

where the block matrix $h_{\text{root}}^{\dagger}$ is the Hermitian conjugate of h_{root}, which is written as

$$h_{\text{root}} = \begin{bmatrix} \sqrt{t_{2y}} & 0 & 0 & \sqrt{t_{2y}}e^{ik_y} \\ 0 & \sqrt{t_{2y}}e^{ik_y} & \sqrt{t_{2y}} & 0 \\ \sqrt{t_{1x}} & 0 & \sqrt{t_{1x}} & 0 \\ \sqrt{t_{2x}}e^{ik_x} & 0 & \sqrt{t_{2x}} & 0 \\ \sqrt{t_{1y}} & 0 & 0 & \sqrt{t_{1y}} \\ 0 & \sqrt{t_{1y}} & \sqrt{t_{1y}} & 0 \\ 0 & \sqrt{t_{1x}} & 0 & \sqrt{t_{1x}} \\ 0 & \sqrt{t_{2x}} & 0 & \sqrt{t_{2x}}e^{ik_x} \end{bmatrix}. \quad (4)$$

H_{root} is a 12×12 matrix since there are 12 sites in each primitive unit cell [see the inset of Fig. 1(c)].

The spectral properties of the descendant SRTI model is studied via numerical calculation for a finite system with 4×4 unit cells, as shown in Fig. 1(d), wherein their spectra are plotted as a function of t_{1x}. Comparing the results in Figs. 1(b) and 1(d), it can be found that the energy spectrum in the parent model is duplicated and rearranged in the descendant model. Meanwhile the topological boundary states are duplicated and rearranged in the descendant model. In particular, the corner states are shifted to finite energies and the number of corner states is doubled, as if
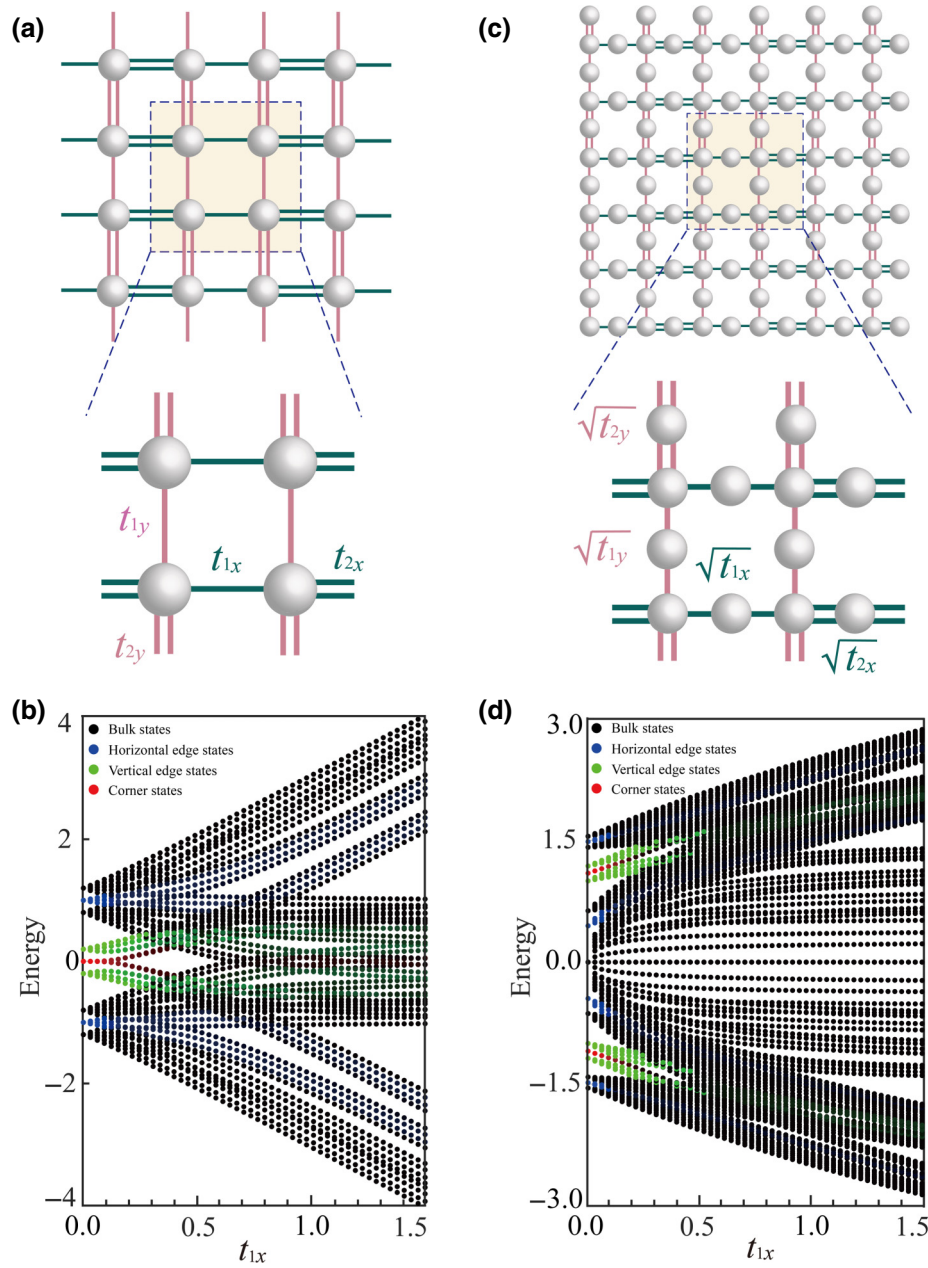
FIG. 1. (a),(c) Tight-binding models of the parent and SRTI lattice. The parent lattice is an asymmetric 2D SSH model (a), while the SRTI is a decorated rectangular lattice model (b). Enlarged images show the structures of the unit cells for (a),(c). Here, the single (double) lines represent the intracell (intercell) couplings. (b),(d) The energy spectra of the finite systems with 4×4 unit cells as functions of t_{1x} in the parent and the descendant models, respectively. In both cases $t_{2x} = 1$, $t_{2y} = 0.2$, and $t_{1y} = t_{1x}$. Various topological boundary states (labeled by different colors) emerge in the topological phase of the parent model and the SRTI. Corner, vertical edge states, and horizontal edge states are characterized by the red, green, and blue colors, separately. The redness of the corner states is connected to the localization of the wave function at the corner unit cells. Similar color schemes are applied to the vertical edge states and horizontal edge states.

the spectrum of the parent model is copied to both the positive and negative energy sectors in the descendant model. To understand such a spectral connection, which is a key feature in the square-root paradigm, one must notice the following relation between the Hamiltonians of the parent and the descendant systems,

$$H_{\text{root}}^2 = \begin{bmatrix} H_{\text{parent}} & 0 \\ 0 & H'_{\text{residual}} \end{bmatrix}. \qquad (5)$$

Here, the diagonal blocks are

$$H_{\text{parent}} = h_{\text{root}}^\dagger h_{\text{root}} = cI_4 + H_{\text{original}} \tag{6}$$

and

$$H'_{\text{residual}} = H_{\text{residual}} + \text{onsite potential} . \tag{7}$$

H_{residual} is the residual Hamiltonian, I_4 is the 4×4 identity matrix, and $c = t_{1x} + t_{1y} + t_{2x} + t_{2y}$ is the constant energy shift. Note that in the Hamiltonian H'_{residual}, the onsite potentials are written as

$$H'_{\text{residual}}(1,1) = H'_{\text{residual}}(2,2) = 2t_{2y}, \tag{8}$$

$$H'_{\text{residual}}(3,3) = H'_{\text{residual}}(7,7) = 2t_{1x}, \tag{9}$$

$$H'_{\text{residual}}(4,4) = H'_{\text{residual}}(8,8) = 2t_{2x}, \tag{10}$$

$$H'_{\text{residual}}(5,5) = H'_{\text{residual}}(6,6) = 2t_{1y}. \tag{11}$$

The full form of H_{residual} is given in the Supplemental Material [50].

Equations (5)–(7) show that the square of the descendant Hamiltonian can be written as the direct sum of the parent Hamiltonian and the residual Hamiltonian (schematically illustrated in in Fig. 2), which dictates the spectral relation between the parent system and the SRTI. This relation thus connects the topological phenomena in the SRTI to those in the parent model.

We notice from the results in Figs. 1(b) and 1(d) that the higher-order topological phases featuring clean spectra of the corner states and edge states (with splitting spectra for the horizontal and vertical edge states) emerge when $t_{1x} < 0.13$.

III. ACOUSTIC METAMATERIAL REALIZATION

We design the acoustic metamaterials as lattices of coupled acoustic cavities to realize the underlying physics of the SRTI model and its parent model. In such designs, the cylindrical acoustic cavities play the role of the sites

in the tight-binding models. The couplings between the sites are realized by the tubes connecting the cylindrical acoustic cavities [see Fig. 3(a)]. The radii of the connecting tubes are carefully designed according to the hopping parameters such that the salient features of the above theoretical models can be delivered to the acoustic metamaterials. These acoustic metamaterials are fabricated using 3D-printing technology based on epoxy. The fabricated epoxy structures, which serve as the hard walls for sound waves, encapsulate the air region in which the acoustic waves propagate. The acoustic wave dynamics in the air region mimics the tight-binding models according to our design. Here, the height and the radius of each cavity are set as $H = 45$ mm and $R = 13$ mm, respectively. The distance between the nearest-neighboring cavities is $d = 48.5$ mm.

The couplings between the nearest-neighboring cavities can be tuned by changing the radii of the tubes connecting the cavities, as elaborated in Fig. 3(a). The intercavity coupling is characterized by the frequency splitting Δf between the odd and the even modes in a system with only two coupled cavities: the intercavity coupling is precisely given by $-\Delta f /2$. This is because such an acoustic system can be mapped into a pair of degenerate sites with intersite coupling of the amplitude $-\Delta f /2$. In Fig. 3(b), the simulated quantitative relation between the intercavity coupling and the tube radius is fitted by a polynomial function, $-\Delta f /2 = 7.025r^2 + 47.155r - 74.387$, where the tube radius r is in units of millimeters.

In the following, the nearest-neighboring coupling amplitudes $t_{2x} = 1$, $t_{2y} = 0.2$, and $t_{1x} = t_{1y} = 0.116$ are considered in both the parent and the descendant models. With these parameters, the nondegenerate vertical and horizontal edge states, and the topological corner states emerge simultaneously. To realize such a regime in the acoustic metamaterials, we design the radii of the tubes to satisfy the following relations for the intercavity couplings: $t_{2x} : t_{2y} : t_{1x} : t_{1y} = 1 : 0.2 : 0.116 : 0.116$ in the parent acoustic metamaterial. In a similar way, the radii of the tubes in the descendant acoustic metamaterial are
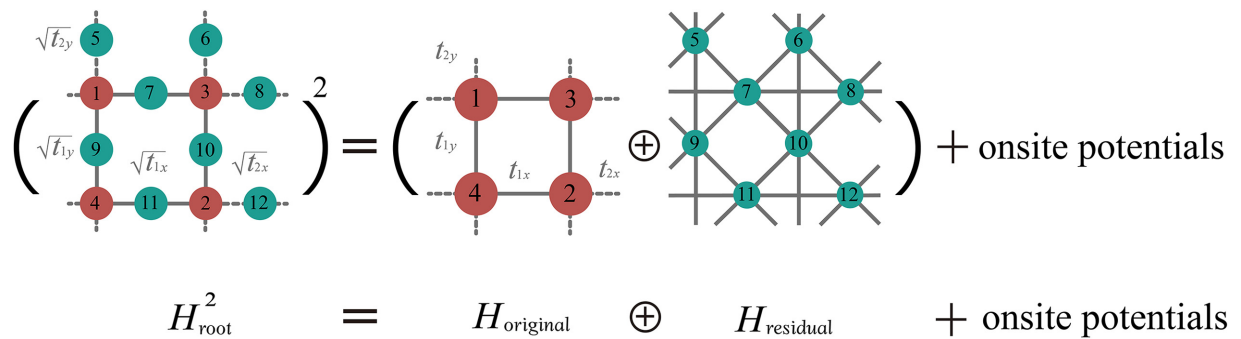

FIG. 2. Schematic illustration of the relation between the SRTI (descendant) model and the original (parent) model. The square of the SRTI Hamiltonian can be decomposed into the original (parent) Hamiltonian, residual Hamiltonian, and onsite potentials.
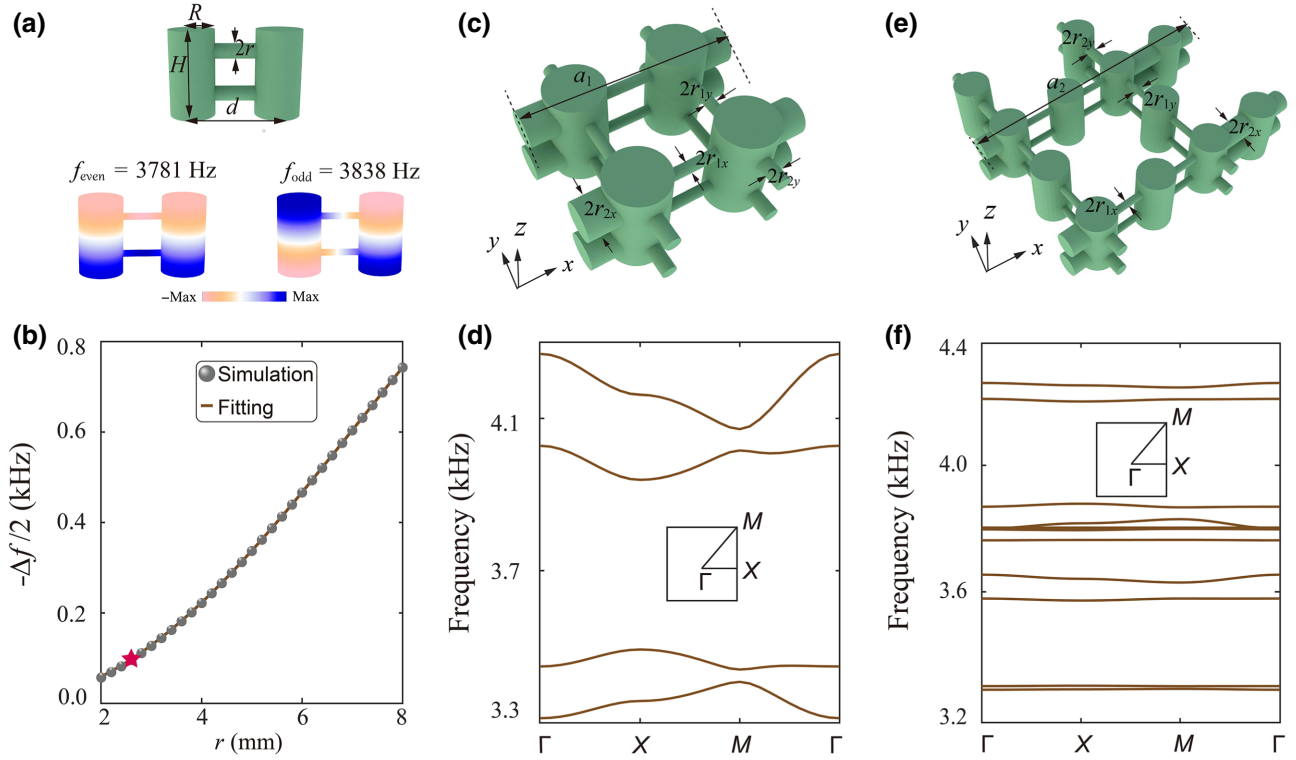
FIG. 3.   (a) Resonant modes in a pair of coupled acoustic cavities. Here, the coupling between the two identical cavities leads to the splitting of the eigenmodes. The hybridized eigenmodes are of even (left) and odd (right) parity, respectively. The frequency difference $\Delta f = f_{even} - f_{odd}$ between the even and odd eigenmodes characterizes the strength of the intercavity coupling, $t = \Delta f / 2$, which can be tuned via the radius of the tubes connecting cavities, as shown in (b). The star labels the tube radius $r = 2.5$ mm for the case in (a). (c) Unit cell of the acoustic metamaterial for the parent model. (d) Acoustic band structure of the acoustic metamaterial in (c). (e) Unit-cell structure of the acoustic metamaterial for the SRTI. (f) Acoustic band structure of the metamaterial in (e). Brillouin zones are shown in the insets of (d),(f). Green regions in (a),(c),(e) are the air regions where the acoustic wave propagates.

designed. Based on the fitted polynomial function between the intercavity coupling and the radius, the radii of the tubes are designed as $r_{1x} = r_{1y} = 2.5$, $r_{2x} = 8$, and $r_{2y} = 3.2$ mm in the parent metamaterial, of which the unit-cell structure is depicted in Fig. 3(c). The lattice constant is chosen as $a_1 = 97$ mm. In the descendant metamaterial, apart from the lattice constant being doubled and becoming $a_2 = 194$ mm, the other geometrical parameters are chosen as $r'_{1x} = r'_{1y} = 4.2$, $r'_{2x} = 8$, and $r'_{2y} = 5$ mm to fulfill the square-root paradigm. Numerical finite-element simulations give the acoustic band structures of the acoustic metamaterials for both the parent model and the descendant SRTI model, and are presented in Figs. 3(d) and 3(f). The large complete acoustic band gaps in Figs. 3(d) and 3(f) enable clear experimental observation of the topological edge and corner states through their spectral properties and wave functions in these acoustic metamaterials.

IV. HIGHER-ORDER TOPOLOGICAL PHENOMENA

We now study the higher-order topological phenomena in the SRTI and its parent system as well as their relations

from both numerical and experimental approaches [see Fig. 4(a) for the experimental sample]. We start by investigating the parent metamaterial. For this purpose, we calculate the spectrum of a finite tight-binding system (acoustic metamaterial) for the parent lattice and present the results in Fig. 4(b) [4(c)]. In both Figs. 4(b) and 4(c), four corner states (red dots) emerge in the spectral gap of the vertical edge states within the bulk band gap. Meanwhile, the horizontal edge states emerge in the two smaller bulk band gaps: the bulk band gap between the first and second bands, and the other between the third and fourth bands. To observe the distribution of the topological edge and corner modes, we perform acoustic pump-probe detections [20,23,51,52].

With the experimental sample shown in Fig. 4(a), we use several pump-probe configurations to detect the spectral properties in the bulk, on the vertical and horizontal edges, and in the corner regions of the sample. In each pump-probe setup, the position of the source (detector) is labeled as S (D) in Fig. 4(a). The colors of these labels denote different setups. In each setup, we use a tiny speaker to generate acoustic waves and use a tiny microphone to detect the acoustic signal. After Fourier transformation
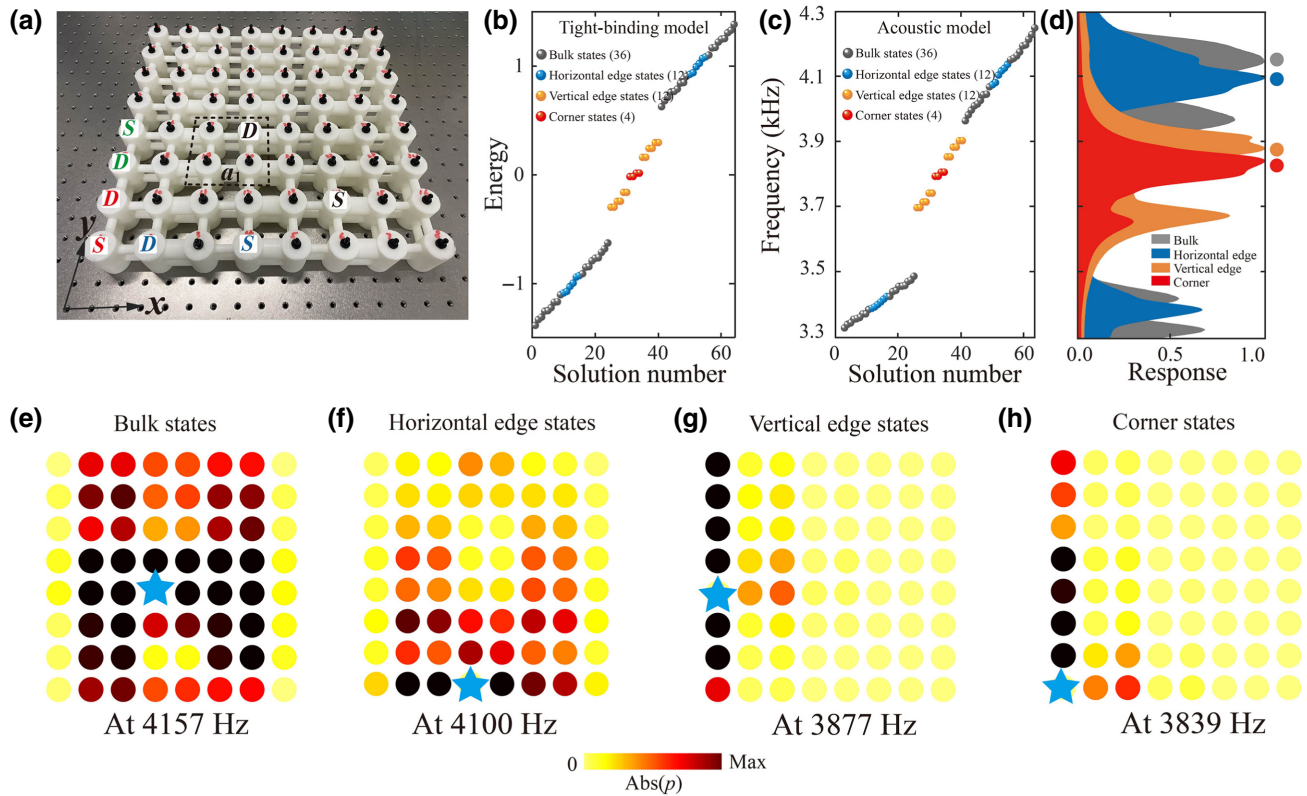
FIG. 4. Experimental observation of the edge and corner states in the acoustic metamaterial for the parent model. (a) Photograph of the acoustic metamaterial. The positions of the sources (*S*) and detectors (*D*) are labeled with different colors for different pump-probe detection schemes: black, green, blue, and red denote the bulk, vertical edge, horizontal edge, and corner pump-probe detection, respectively. (b) Energy spectrum of a finite tight-binding system with 4×4 unit cells. The bulk, vertical edge, horizontal edge, and corner states are labeled with black, orange, blue, and red colors. The numbers in brackets give the numbers of each type of eigenstate. (c) Acoustic spectrum of a finite acoustic metamaterial with 4×4 unit cells. (d) Measured acoustic signals (absolute value of the acoustic pressure) in various pump-probe detection schemes. Each curve is normalized so that the maximum is 1. (e)–(h) Measured acoustic wave amplitude (i.e., absolute value of the acoustic pressure p) profiles for the bulk states (e), horizontal edge states (f), vertical edge states (g), and corner states (h) at various excitation frequencies [these frequencies are also indicated by the colored dots in (d)]. Blue stars in (e)–(h) label the source positions.

of the collected acoustic signals, we obtain the pump-probe responses in the frequency domain. The speaker and the microphone are inserted into the cavities labeled in Fig. 4(a). The detected acoustic signals, which are proportional to the acoustic pressures in the detection cavity, are retrieved and analyzed by an Agilent network analyzer.

The measured pump-probe responses in Fig. 4(d) show excellent consistency with the calculated acoustic spectrum in Fig. 4(c). In particular, the resonance due to the corner mode emerges in the spectral gap of the vertical edge modes inside the bulk gap. To further confirm experimentally the emergence of the topological edge and corner states, we also use a tiny speaker to excite the acoustic waves in the source positions labeled in Fig. 4(a) but now move the microphone to detect the acoustic signals in all cavities (one by one) except in the source cavity. With such a method, we measure the acoustic wave patterns of the bulk, vertical edge, horizontal edge, and the

corner states at their resonant frequencies [i.e., when we measure, e.g., the vertical edge states, we set the excitation frequency as a resonant frequency in the vertical edge response curve in Fig. 4(d)]. From the measured acoustic wave patterns in Figs. 4(e)–4(h), one can directly recognize the wave patterns of the bulk, edge, and corner modes. These results confirm the coexistence of the bulk, edge, and corner states, and thus verify that the parent system is an acoustic higher-order topological insulator with special spectral properties that are consistent with the calculations.

In the following, we proceed to study the higher-order topological phenomenon in the SRTI acoustic metamaterial via both experimental and numerical approaches. The sample of the SRTI acoustic metamaterial is shown in Fig. 5(a) where we label the source (*S*) and detector (*D*) positions for the bulk, the vertical edge, the horizontal edge, and the corner pump-probe configurations using different colors. The measured pump-probe responses are
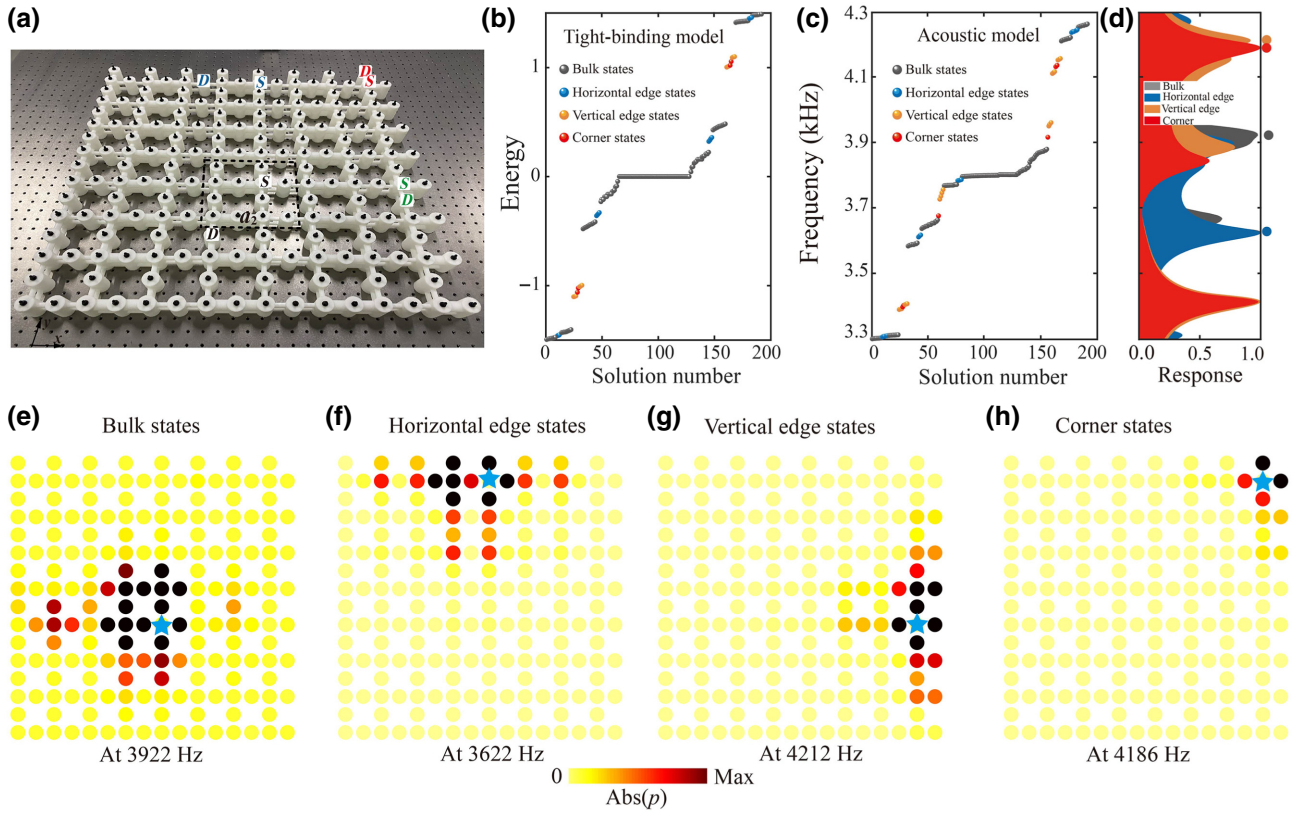
FIG. 5. Experimental observation of the edge and corner states in the acoustic metamaterial for the SRTI. (a) Photograph of the SRTI acoustic metamaterial. The positions of the sources (*S*) and detectors (*D*) are labeled with different colors for different pump-probe detection schemes: black, green, blue, and red denote the bulk, vertical edge, horizontal edge, and corner pump-probe configurations, respectively. (b) Energy spectrum of a finite tight-binding system with 4 × 4 unit cells. (c) Acoustic spectrum of a finite SRTI acoustic metamaterial with 4 × 4 unit cells. (d) Measured acoustic signals (proportional to the absolute value of the acoustic pressure) in various pump-probe configurations. Each curve is normalized so that its maximum is 1. (e)–(h) Measured acoustic wave amplitude (proportional to the absolute value of the acoustic pressure) profiles for the bulk states (e), horizontal edge states (f), vertical edge states (g), and corner states (h) at their resonant frequencies [these frequencies are also indicated by the colored dots in (d)]. Blue stars in (e)–(h) label the source positions.

compared with the acoustic spectrum from numerical simulations. For this purpose, we first calculate the spectrum of a finite SRTI lattice with 4 × 4 unit cells in both the tight-binding model and the acoustic metamaterial. The calculated spectra are presented in Figs. 5(b) and 5(c). The acoustic spectrum mimics the tight-binding spectrum and produces the desired spectral connection between the SRTI and its parent model. This observation supports our study of the square-root topological phases using acoustic metamaterials. Moreover, the emergence of the edge and corner states in these calculations offers guidance to their experimental detections.

Using the acoustic pump-probe configurations labeled in Fig. 5(a), we measure the pump-probe responses in the bulk, the vertical edge, the horizontal edge, and the corner regions. The measured responses in Fig. 5(d) show excellent consistency with the simulated acoustic spectrum in Fig. 5(c), despite the slight frequency blue shifts in the

measurements, which may be due to fabrication imperfections in the metamaterial. We further use acoustic pump probes to detect the acoustic wave patterns for the bulk states, the horizontal edge states, the vertical edge states, and the corner states. Here, we fix the source, and their positions are indicated in Fig. 5(a), and move the detector to probe the acoustic signals in all other cavities when the excitation frequency is at the resonant frequencies in the curves in Fig. 5(d) for each kind of eigenstate. For instance, to detect the wave pattern of the corner states, we set the excitation frequency as 4186 Hz. The measured wave patterns of the bulk, the horizontal edge, the vertical edge, and the corner states are shown in Figs. 5(e)–5(h). These wave patterns indeed show obvious features of the bulk, the horizontal edge, the vertical edge, and the corner states, confirming the emergence of the multidimensional topological states as a key feature of the higher-order topology in the SRTI metamaterial.
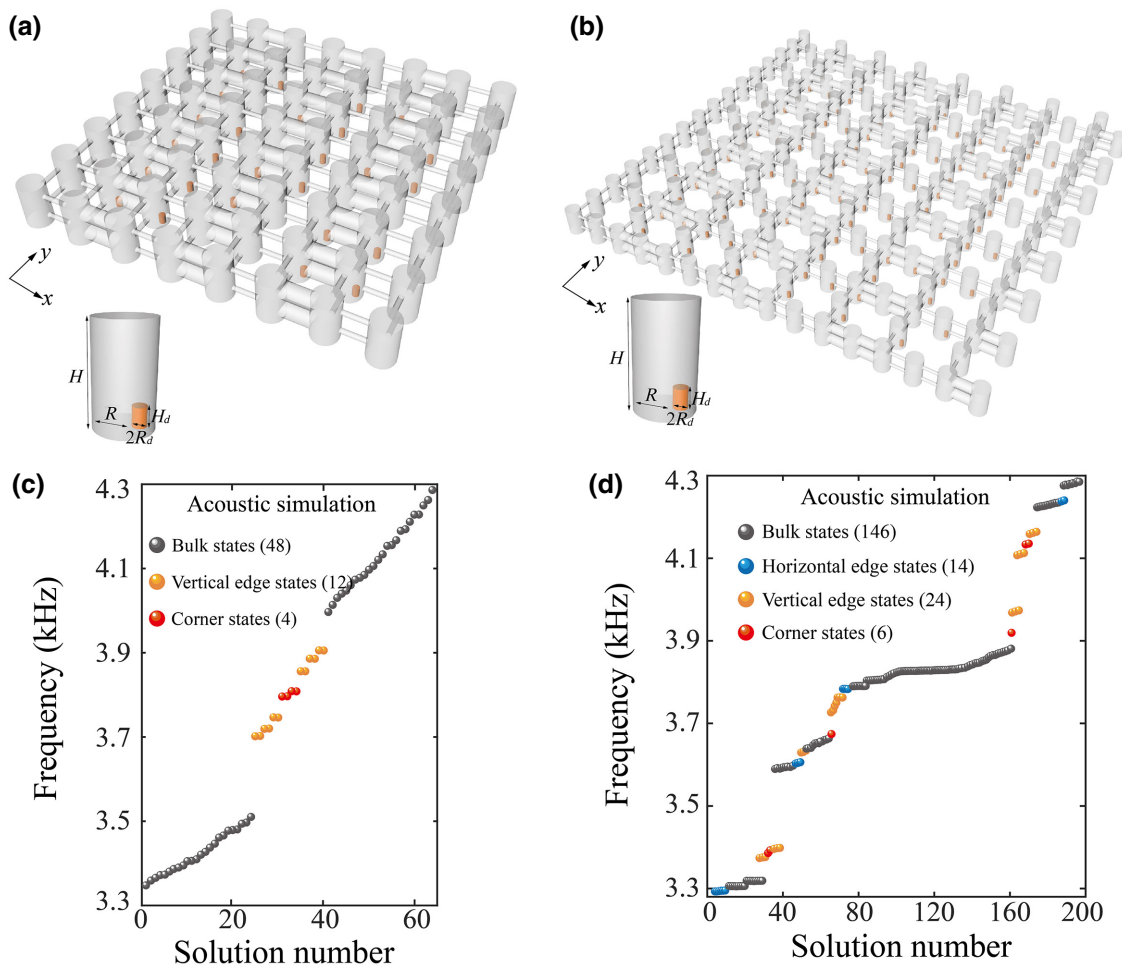
FIG. 6.   Robustness of the topological edge and corner states. (a),(b) Acoustic metamaterials of (a) the parent and (b) the SRTI with defects introduced to the cavities in the bulk region. Lower-left in (a),(b) A close look at the geometry inside a cavity with a defect (the yellow pillar). (c),(d) Simulated acoustic spectrum for the acoustic metamaterial with defects for (c) parent model and (d) SRTI.

V. ROBUSTNESS OF THE TOPOLOGICAL EDGE AND CORNER STATES

To demonstrate the robustness of the topological edge and corner states in the two acoustic metamaterials studied previously, we deliberately introduce defects and study their effects on the acoustic states using numerical simulations. As illustrated in Figs. 6(a) and 6(b), the defects are mimicked by randomly introducing the yellow epoxy pillars with a radius $R_d = 3.25$ mm and a height $H_d = 9$ mm in some cavities. These pillars at the bottom of these cavities lead to a frequency shift in the cavity modes and thus serve as the additional random onsite potential energy for the acoustic modes. Acoustic simulations, however, indicate that the main features of the spectrum and the wave functions, i.e., the emergence of the edge and corner states in the bulk spectral gap, are not modified, despite introducing these defects. Changing the pillars in a series of parameter ranges does not change this observation (see Supplemental Material [50] for more simulation

data). These simulation results indicate the robustness of the topological edge and corner states.

VI. CONCLUSION AND OUTLOOK

In this work, we demonstrate the emergence of higher-order topological phenomena in square-root topological phases based on rectangular-lattice acoustic metamaterials. Here, the controllable couplings among the acoustic cavities via tuning the radii of the tubes connecting them are favorable for the realization of the square-root scheme. With consistent experiments and simulations, we verify that both the parent model and the SRTI are higher-order topological insulators with coexisting edge and corner states. Furthermore, we show that the spectral features of the parent model and the SRTI are connected via the square-root relations. Both the parent model and the SRTI have splitting horizontal and vertical edge states with dispersions unique to the rectangular SRTIs. Our work provides an unconventional scheme towards SRTIs that can

be generalized to other systems, such as electrical circuits, mechanical, and photonic systems, that may inspire future exploration of square-root topology. The application of such square root topology in, e.g., photonic systems, may offer unconventional schemes for robust light guiding and trapping [32,53]. Such applications are particularly appealing for the systems studied here and the like, because the couplings here can be tuned in a large parameter range and the splitting between the horizontal and vertical edge states gives more possibilities in the manipulation of wave dynamics in such systems.

Furthermore, exploiting space-coiled-up cavities [54, 55] in place of the cylindrical cavities would enable topological manipulation of acoustic waves in the deep-subwavelength regime [54,55], which is attractive for applications. Moreover, it is very interesting and worthwhile to ask whether the square-root approach can be generalized to other lattices with different symmetries [56]. This may be possible because the square-root principle is based on local structure modifications and can in principle be generalized to other lattices. Meanwhile, higher-order topology and topological transitions exist in various lattice systems [57,58]. It is thus possible to generalize the square root higher-order phase studied here to other lattices and systems, which is a topic worth exploring in the future.

[1] D. J. Thouless, M. Kohmoto, M. P. Nightingale, and M. den Nijs, Quantized Hall Conductance in a Two-Dimensional Periodic Potential, Phys. Rev. Lett. **49**, 405 (1982).

[2] M. Z. Hasan and C. L. Kane, Colloquium: Topological insulators, Rev. Mod. Phys. **82**, 3045 (2010).

[3] X. Qi and S. Zhang, Topological insulators and superconductors, Rev. Mod. Phys. **83**, 1057 (2011).

[4] C. L. Kane and E. J. Mele, Quantum Spin Hall Effect in Graphene, Phys. Rev. Lett. **95**, 226801 (2005).

[5] C. L. Kane and E. J. Mele, Z_2 Topological Order and the Quantum Spin Hall Effect, Phys. Rev. Lett. **95**, 146802 (2005).

[6] B. A. Bernevig, T. L. Hughes, and S. Zhang, Quantum spin Hall effect and topological phase transition in HgTe quantum wells, Science **314**, 1757 (2006).

[7] X. Qi and S. Zhang, The quantum spin Hall effect and topological insulators, Phys. Today **63**, 33 (2010).

[8] L. H. Wu and X. Hu, Scheme for Achieving a Topological Photonic Crystal by Using Dielectric Material, Phys. Rev. Lett. **114**, 223901 (2015).

[9] L. Xu, H. Wang, Y. Xu, H. Chen, and J. Jiang, Accidental degeneracy in photonic bands and topological phase transitions in two-dimensional core-shell dielectric photonic crystals, Opt. Express **24**, 18059 (2016).

[10] C. He, X. Ni, H. Ge, X. Sun, Y. Chen, M. Lu, X. Liu, and Y. Chen, Acoustic topological insulator and robust one-way sound transport, Nat. Phys. **12**, 1124 (2016).

[11] Z. Zhang, Q. Wei, Y. Cheng, T. Zhang, D. Wu, and X. Liu, Topological Creation of Acoustic Pseudospin Multipoles in a Flow-Free Symmetry-Broken Metamaterial Lattice, Phys. Rev. Lett. **118**, 084303 (2017).

[12] S. Wu, Y. Wu, and J. Mei, Topological helical edge states in water waves over a topographical bottom, New J. Phys. **20**, 023051 (2018).

[13] W. A. Benalcazar, B. A. Bernevig, and T. L. Hughes, Quantized electric multipole insulators, Science **357**, 61 (2017).

[14] W. A. Benalcazar, B. A. Bernevig, and T. L. Hughes, Electric multipole moments, topological multipole moment pumping, and chiral hinge states in crystalline insulators, Phys. Rev. B **96**, 245115 (2017).

[15] Z. Song, Z. Fang, and C. Fang, $(d-2)$-Dimensional Edge States of Rotation Symmetry Protected Topological States, Phys. Rev. Lett. **119**, 246402 (2017).

[16] F. Schindler, A. M. Cook, M. G. Vergniory, Z. Wang, S. S. P. Parkin, B. Andrei Bernevig, and T. Neupert, Higher-order topological insulators, Sci. Adv. **4**, 3466 (2018).

[17] M. Serra-Garcia, V. Peri, R. Süsstrunk, O. R. Bilal, T. Larsen, L. G. Villanueva, and S. D. Huber, Higher-order topological insulators, Nature **555**, 342 (2018).

[18] X. Ni, M. Weiner, A. Alù, and A. B. Khanikaev, Observation of higher-order topological acoustic states protected by generalized chiral symmetry, Nat. Mater. **18**, 113 (2018).

[19] B. Xie, H. Wang, H. Wang, X. Zhu, J. Jiang, M. Lu, and Y. Chen, Second-order photonic topological insulator with corner states, Phys. Rev. B **98**, 205147 (2018).

[20] X. Zhang, H. Wang, Z. Lin, Y. Tian, B. Xie, M. Lu, Y. Chen, and J. Jiang, Second-order topology and multidimensional topological transitions in sonic crystals, Nat. Phys. **15**, 582 (2019).

[21] M. Serra-Garcia, R. Süsstrunk, and S. D. Huber, Observation of quadrupole transitions and edge mode topology in an LC circuit network, Phys. Rev. B **99**, 020304 (2019).

[22] H. Xue, Y. Yang, F. Gao, Y. Chong, and B. Zhang, Acoustic higher-order topological insulator on a kagome lattice, Nat. Mater. **18**, 108 (2019).

[23] X. Zhang, Z. Lin, H. Wang, Z. Xiong, Y. Tian, M. Lu, Y. Chen, and J. Jiang, Symmetry-protected hierarchy of anomalous multipole topological band gaps in nonsymmorphic metacrystals, Nat. Commun. **11**, 65 (2020).

[24] X. Zhou, Z. K. Lin, W. Lu, Y. Lai, B. Hou, and J. H. Jiang, Twisted quadrupole topological photonic crystals, Laser Photonics Rev. **10**, 1002 (2020).

[25] L. He, Z. Addison, E. J. Mele, and B. Zhen, Quadrupole topological photonic crystals, Nat. Commun. **11**, 3119 (2020).

[26] H. Xue, Y. Ge, H. Sun, Q. Wang, D. Jia, Y. Guan, S. Yuan, Y. Chong, and B. Zhang, Observation of an acoustic octupole topological insulator, Nat. Commun. **11**, 2442 (2020).

[27] Y. Qi, C. Qiu, M. Xiao, H. He, M. Ke, and Z. Liu, Acoustic Realization of Quadrupole Topological Insulators, Phys. Rev. Lett. **124,** 206601 (2020).

[28] Q. Wei, X. Zhang, W. Deng, J. Lu, X. Huang, M. Yan, G. Chen, Z. Liu, and S. Jia, Higher-order topological semimetal in acoustic crystals, Nat. Mater. **20,** 812 (2021).

[29] S. Wu, B. Jiang, Y. Liu, and J. Jiang, All-dielectric photonic crystal with unconventional higher-order topology, Photonics Res. **9,** 668 (2021).

[30] L. Luo, H. Wang, Z. Lin, B. Jiang, Y. Wu, F. Li, and J. Jiang, Observation of a phononic higher-order Weyl semimetal, Nat. Mater. **20,** 794 (2021).

[31] J. Arkinstall, M. H. Teimourpour, L. Feng, R. El-Ganainy, and H. Schomerus, Topological tight-binding models from nontrivial square roots, Phys. Rev. B **95,** 165109 (2017).

[32] M. Kremer, I. Petrides, E. Meyer, M. Heinrich, O. Zilberberg, and A. Szameit, A square-root topological insulator with non-quantized indices realized with photonic Aharonov-Bohm cages, Nat. Commun. **11,** 907 (2020).

[33] M. Yan, X. Huang, L. Luo, J. Lu, W. Deng, and Z. Liu, Acoustic square-root topological states, Phys. Rev. B **102,** 180102 (2020).

[34] L. Song, H. Yang, Y. Cao, and P. Yan, Realization of the square-root higher-order topological insulator in electric circuits, Nano Lett. **20,** 7566 (2020).

[35] T. Mizoguchi, Y. Kuno, and Y. Hatsugai, Square-root higher-order topological insulator on a decorated honeycomb lattice, Phys. Rev. A **102,** 033527 (2020).

[36] T. Mizoguchi, T. Yoshida, and Y. Hatsugai, Square-root topological semimetals, Phys. Rev. B **103,** 045136 (2020).

[37] M. Ezawa, Systematic construction of square-root topological insulators and superconductors, Phys. Rev. Res. **2,** 33397 (2020).

[38] A. M. Marques and R. G. Dias, 2^n-root weak, Chern, and higher-order topological insulators, and $2n$-root topological semimetals, Phys. Rev. B **104,** 165410 (2021).

[39] J. Kang, T. Liu, M. Yan, D. Yang, X. Huang, R. Wei, J. Qiu, G. Dong, Z. Yang, and F. Nori, arXiv:2109.00879 (2021).

[40] A. M. Marques, L. Madail, and R. G. Dias, One-dimensional 2^n-root topological insulators and superconductors, Phys. Rev. B **103,** 235425 (2021).

[41] W. Yan, D. Song, S. Xia, J. Xie, L. Tang, J. Xu, and Z. Chen, Realization of second-order photonic square-root topological insulators, ACS Photonics **8,** 3308 (2021).

[42] Z. Lin, S. Ke, X. Zhu, and X. Li, Square-root non-Bloch topological insulators in non-Hermitian ring resonators, Opt. Express **29,** 8462 (2021).

[43] T. Yoshida, T. Mizoguchi, Y. Kuno, and Y. Hatsugai, Square-root topological phase with time-reversal and particle-hole symmetry, Phys. Rev. B **103,** 235130 (2021).

[44] H. Wu, G. Wei, Z. Liu, and J. Xiao, Square-root topological state of coupled plasmonic nanoparticles in a decorated Su–Schrieffer–Heeger lattice, Opt. Lett. **46,** 4256 (2021).

[45] Z. Geng, Y. Peng, H. Lv, Z. Xiong, Z. Chen, and X. Zhu, Square-root-like higher-order topological states in three-dimensional sonic crystals, J. Phys.: Condens. Matter **34,** 104001 (2021).

[46] S. Yang, J. H. Page, Z. Liu, M. L. Cowan, and C. T. Chan, Ultrasound Tunneling through 3D Phononic Crystals, Phys. Rev. Lett. **88,** 104301 (2002).

[47] S. X. Yang, J. H. Page, Z. Y. Liu, M. L. Cowan, C. T. Chan, and P. Sheng, Focusing of Sound in a 3D Phononic Crystal, Phys. Rev. Lett. **93,** 024301 (2004).

[48] M. Xiao, W. Chen, W. He, and C. T. Chan, Synthetic gauge flux and Weyl points in acoustic systems, Nat. Phys. **11,** 920 (2015).

[49] C. He, H. Lai, B. He, S. Yu, X. Xu, M. Lu, and Y. Chen, Acoustic analogues of three-dimensional topological insulators, Nat. Commun. **11,** 2318 (2020).

[50] See Supplemental Material http://link.aps.org/supplemental/10.1103/PhysRevApplied.19.024023 for further theoretical analysis, numerical calculations, and experimental data.

[51] B. Jiang, A. Bouhon, Z. Lin, X. Zhou, B. Hou, F. Li, R. Slager, and J. Jiang, Experimental observation of non-Abelian topological acoustic semimetals and their phase transitions, Nat. Phys. **17,** 1239 (2021).

[52] S. Wu, Z. Lin, B. Jiang, X. Zhou, Z. H. Hang, B. Hou, and J. Jiang, Higher-order Topological States in Acoustic Twisted Moiré Superlattices, Phys. Rev. Appl. **17,** 034061 (2022).

[53] W. Yan, D. Song, S. Xia, J. Xie, Liqin Tang, J. Xu, and Z. Chen, Realization of second-order photonic square-root topological insulators, arXiv:2110.05091.

[54] Z. Liang and J. Li, Extreme Acoustic Metamaterial by Coiling Up Space, Phys. Rev. Lett. **108,** 114301 (2012).

[55] C. Liu, J. Shi, W. Zhao, X. Zhou, C. Ma, R. Peng, M. Wang, Z. Hang, X. Liu, J. Christensen, *et al.*, Three-Dimensional Soundproof Acoustic Metacage, Phys. Rev. Lett. **127,** 084301 (2021).

[56] H. Chu, Y. Zhang, J. Luo, C. Xu, X. Xiong, R. Peng, M. Wang, and Y. Lai, Band engineering method to create Dirac cones of accidental degeneracy in general photonic crystals without symmetry, Opt. Express **12,** 18070 (2021).

[57] B. Xie, H.-X. Wang, X. Zhang, P. Zhan, J.-H. Jiang, M. Lu, and Y. Chen, Higher-order band topology, Nat. Rev. Phys. **3,** 520 (2021).

[58] Z. Lin and J. Jiang, Dirac cones and higher-order topology in quasi-continuous media, Europhys. Lett. **137,** 15001 (2022).